Journal of Materials Chemistry C

ROYAL SOCIETY OF CHEMISTRY

PAPER

View Article Online
View Journal | View Issue

Cite this: J. Mater. Chem. C, 2020, 8, 16992

Dipolar cation accumulation at the interfaces of perovskite light-emitting solar cells†

D. S. Gets, *[a] G. A. Verkhogliadov,[a] E. Y. Danilovskiy,[a] A. I. Baranov,[b] S. V. Makarov [a] and A. A. Zakhidov*[ac]

Received 5th June 2020,
Accepted 22nd October 2020

DOI: 10.1039/d0tc02654a

rsc.li/materials-c

Ionic migration plays an important role in the operation of perovskite-based solar cells and light-emitting diodes. Although ionic migration is a reversible process, it often leads to worsening of the perovskite-based device performance and hysteresis in current–voltage characteristics; the phase segregation in mixed halide perovskites is the most harmful effect. The reason lies in the dynamical band structure changes, one of the biggest challenges in the development of light-emitting solar cells, which can be solved through controllable engineering. Herein, we demonstrate the controllable band structure bending due to ion migration under an applied voltage in mixed halide perovskite devices. The band structure rearrangement is demonstrated in light-emitting solar cells based on the perovskite with organic cations methylammonium (MA^+) and formamidinium (FA^+), and with PEDOT:PSS and C60 transport layers having a high barrier of 0.8 eV for charge injection. The devices based on $MAPbBr_2I$ and $FAPbBr_2I$ demonstrate different threshold voltages of 1.7 and 2.6 V, respectively, in the LED regime after device pre-biasing, whereas the device with the monohalide perovskite $MAPbBr_3$ does not demonstrate such behavior. We assume that this arises from the different dipole moments of the organic cation molecules, MA^+ and FA^+, possessing non-zero dipole moments of 2.29 Debye and 0.21 Debye, respectively. Our hypothesis is that under the applied voltage, perovskite cations and anions move towards the perovskite/transport layer interfaces and form accumulation layers. Moreover, the organic accumulation layer at the perovskite/electron transport layer interface additionally bends the device band structure and lowers the LED threshold voltage due to its dipole nature. This ability to change the device band structure *in situ* opens the way for the development of dual functional devices based on a simple design. In addition, it makes the mixed halide perovskite more flexible than monohalide ones for the creation of different optoelectronic devices without the use of special types of transport materials.

Introduction

Organo-halide perovskites are a prospective family of organic–inorganic materials for the development of highly efficient solar cells (SCs)[1,2] and light-emitting diodes (LEDs).[3,4] The perovskites have high absorption coefficients, high exciton binding energies, wide band gap tunability and solution processing ability.[5–9] SCs based on perovskites have reached the efficiencies of SCs produced by well-established technologies like silicon.[10] Perovskite LEDs have also demonstrated high efficiencies, as well as narrow luminescence line widths and high color rendering indexes.[11] However, the perovskites demonstrate some undesirable effects like ionic migration, which tremendously affect the device performance.[12,13] The ionic migration is induced either by light illumination[14] or by applying high current densities[15] in the devices, and is most clearly manifested in the mixed halide perovskites where it results in anion segregation.[12,14] Perovskite ions and their vacancies have low activation energies that make them movable even at room temperature. For a long time, the ionic migration has remained one of the biggest problems of perovskite devices.[16–21] The ionic migration strongly affects the device performance and results in hysteresis of the PV parameters.[22] It is clearly seen in the current–voltage characteristic (J–V) of the perovskite-based solar cells, where the efficiency depends on the direction of the voltage sweep. This unwanted behavior can be slowed down in different ways, such as the use of multiple cation compositions, increasing the perovskite crystallinity, decreasing the amount of defects in the perovskite grains and stabilization of interfaces.[23–27]

[a] ITMO University, Department of Physics and Engineering, Lomonosov Str. 9, Saint-Petersburg 191002, Russia. E-mail: dmitry.gets@metalab.ifmo.ru, zakhidov@utdallas.edu
[b] St Petersburg Academic University, ul. Khlopina 8/3a, St Petersburg 194021, Russia
[c] Alan G. MacDiarmid NanoTech Institute, Department of Physics, University of Texas at Dallas, Richardson, TX 75083, USA

† Electronic supplementary information (ESI) available. See DOI: 10.1039/d0tc02654a

Despite all of the negative effects of ionic migration, it can demonstrate some useful functionality. For example, under light illumination or voltage application voltage, the perovskite ions move towards the electron and hole transport layers (ETL and HTL), thus forming the p–i–n structure inside the perovskite layer.[20,28–31] This p–i–n structure is responsible for the temporal performance enhancement of solar cells, which is known as light-induced self-poling effect,[28] and the possibility of the creation of dual functional devices – light emitting solar cells (LESC).[32–34] The latest experimental investigations of ionic migration in $MAPbI_3$ showed that the anion has the greatest diffusion coefficient and the cation stays almost intact,[35,36] which means that the p–i–n structure inside the perovskite layer is formed mostly due to halogen ion migration. The possibility of the p–i–n structure formation due to the ion migration inside the perovskite layer is beneficial for the development of the LESC.

The main problem of LESC is the absence of a mechanism to change the device band structure *in situ* to achieve a certain working regime – LED or SC, resulting in additional carrier losses due to the poor band alignment between the transport layers and emission layer. Hence, the creation of LESC with high efficiencies of both working regimes is a big challenge. Usually, to overcome the potential barriers for charge injection in the SC device design, it is necessary to insert additional layers to adjust the work function of the electrode. There are several examples of different perovskite LESCs[37–39] based on either polyelectrolyte transport material or low work function electrode material.[33,34] In the case of the high potential barrier, the polyelectrolyte transport material could reach PCE $\approx$ 1% and $EQE_{EL} \approx 0.12\%$,[33] whereas the performance is PCE $\approx$ 12% and $EQE_{EL} \approx 0.04\%$[34] for the case of the low potential barrier and low work function materials. However, the use of these additional layers results in higher device complexity or higher instability due to electrode chemical reactivity. Finding a simple way to conveniently adjust for the SC device band structure to work as a LED is a challenge.

In this work, we demonstrate controllable real time band bending of the perovskite LESC based on mixed halide perovskites, which can be caused by dipole layer formation from perovskite cation ions. Mixed halide perovskites demonstrate more pronounced ionic migration as compared to monohalide ones, because of the halide segregation accelerating a movement of the cations and anions under an external electric field. The difference in the ionic migration is demonstrated by a high change in the LED threshold voltage (V_{th}) and built-in voltage (V_{bi}) values after pre-biasing the device at different biasing voltages (V_b). We assume that the pre-biasing results in the migration of Br^- and I^- ions towards the PEDOT:PSS/perovskite interface, and the MA^+ and FA^+ molecules migrate towards the perovskite/C_{60} interface, forming the accumulation layers there. The presence of these accumulation layers at the perovskite interfaces leads to p–i–n structure formation inside the perovskite layer. Since the molecules of the perovskite organic cations (MA^+ and FA^+) have non-zero dipole moments (2.29 and 0.21 Debye),[40] that cation accumulation layer at the perovskite interface will more efficiently bend the device band structure in the LED operation mode. This leads to an improvement of the charge injection conditions with consequent V_{th} lowering down to 1.7 V and increasing the optical power output.

Results and discussion

To create an efficient LESC, it is essential to tune the potential barriers between the perovskite and transport layers. Generally, the LEDs and SCs perform reciprocal functions of converting the electrical power to light and *vice versa*. Although these devices share similar designs, their designs are tuned in a specific way to maximize the performance of their primary functions. In addition, the reciprocal function is greatly suppressed by the design due to additional losses because of the high band mismatch. Therefore, in order to create an efficient LESC, an approach to adjust the band diagram for a specific working regime should be found. However, the dual functionality in the perovskite-based devices was realized throughout the one-way modification of potential barriers either by use of a low work function electrode material[34] or use of special transport material with polyelectrolyte properties.[33] The first two approaches are based on the modulation of transport material properties. In the first case, the potential barrier for charge injection was overcome due to the initially tuned device structure by use of the low work function electrode material calcium.[34] In the second case, the potential barrier was lowered by the use of polyethylenimine or pre-doped polyethylenimine (PEI or $PEIBim_4$) as an ETL.[33] It is important to note that PEI demonstrates polyelectrolyte properties, which offers internal dipole formation. It is also usually used as a universal buffer layer to lower the electrode work function.[41] The presence of dipoles at the interface $MAPbBr_3$/ETL bends the band structure. Therefore, the potential barrier for the charge injection lowers. That allows for achieving relatively good PV and LED performance in the same device.

Additionally, there is a third approach to utilize ion movement inside the perovskite layer.[32] The device design used in these devices is suitable for SC operation, but it is suboptimal for LED operation. The main problem is the high potential barrier for electron injection ($\approx$0.8 eV) between the perovskite and ETL, which makes this device design highly undesirable for LED realization. In this case, under an applied external voltage, the perovskite ions move towards the perovskite-transport layer interfaces and form a p–i–n structure inside the perovskite. This p–i–n structure inside the perovskite layer supports the dual functionality, and it allows for tuning of the reversible device band structure because it can be released by removal of the external voltage. Sustaining and releasing the p–i–n structure inside the perovskite layer are the most crucial effects for LESC operation.

To investigate a beneficial effect of the ionic migration and p–i–n structure development inside the perovskite layer for band bending, the two perovskite organic cations FA^+ and MA^+ were chosen. The $MAPbBr_2I$ perovskite has a slightly wider

band gap than $FAPbBr_2I$. In addition, the FA^+ cation provides higher stability than MA^+, but it is most important that they have high dipole moments of 2.29 and 0.21 Debye,[40] respectively. Therefore, this high difference in the dipole moments should manifest in the dual functionality. To precisely investigate the performance of the dual functional devices upon cation composition in the mixed halide perovskite, the devices with cation $FA_xMA_{1-x}PbBr_2I$ were created (x = 0, 0.2, 0.4, 0.6, 0.8, 1). The obtained perovskite devices were tested for solar cell performance, and they all demonstrated the following PV characteristics: $V_{OC} \approx$ 0.85–1 V, $J_{SC} \approx$ 8–10 mA cm^{-2}, FF $\approx$ 50%, PCE $\approx$ 4% (Fig. S1, ESI†). Investigation of the device LED regime performance and p–i–n structure formation was conducted by a slightly modified procedure proposed elsewhere.[32]

Each obtained LESC device was subjected to a sequence of voltage biasing cycles at a certain biasing voltage (V_b = 1, 1.5, 2 V) for 1 minute in the dark with the following immediate measurement of the J–V characteristic from V_b up to 3–4 V. As a result, the MA- and FA-based perovskite devices demonstrated a great difference in the J–V characteristics after the pre-biasing at V_b = 1.5 V (Fig. 1a). The applying of an external electric field to the device led to the following two processes: the first one is the movement and accumulation of perovskite ions at the interfaces perovskite/ETL and perovskite/HTL, and the second one is the current-induced segregation.[15] The presence of an excess of perovskite ions at the interfaces led to p–i–n structure formation inside the perovskite layer since the additional ions at the interfaces serve as dopants.[20,28,42] A higher V_b should result in higher ion density at the perovskite interface, which in turn results in a strongly pronounced p–i–n structure. However, ionic migration, as well as p–i–n structure formation and segregation, are temporal effects. In addition, the removal of an external electric field leads to the reverse redistribution of the ions inside the perovskite layer and disappearance of the p–i–n junction. Therefore, to achieve low V_{th}, the device always has to be under an applied external voltage maintaining the p–i–n structure inside the perovskite layer. Along with J–V, we also measured the electroluminescence (EL) spectra of the LED at different voltages (insets in Fig. 2, and Fig. S2, ESI†). It also demonstrated a shift in the low voltage region upon voltage pre-biasing, which correlates with the behavior of the J–V characteristics. We deduced V_{th} values from the zero-crossing of the J–V curve linear approximation (Fig. S2, ESI†).

Fig. 1a shows the J–V characteristics of the devices based on the MA- and FA-based perovskite after several pre-biasings at 1.5 V. The J–V characteristics demonstrate a clear difference in the position of the "kink" after the pre-biasing of the device at 1.5 V for 1 minute. Namely, the obtained V_{th} values for the MA-based ($V_{th} \approx$ 1.68 V) and FA-based ($V_{th} \approx$ 2.62 V) perovskites demonstrate different values of V_{th} (difference is $\Delta V_{th} \approx$ 1 V), which reflects the dependence of the device band bending on the cation composition. As shown in Fig. 1b, the use of the mixed cation composition FA_xMA_{1-x} ($0 \leq x \leq 1$) in the perovskite demonstrates a non-linear dependence of V_{th} on the cation composition, where the V_{th} values were obtained for different cation compositions FA_xMA_{1-x} (where x = 0, 0.2, 0.4, 0.6, 0.8, 1) after the pre-biasing at V_b = 1.5 V. Although the FA-based perovskites demonstrate high V_{th} value, it can be further lowered by pre-biasing the device at higher voltages. Fig. 2a shows the J–V curves of the FA-based LESC measured after the pre-biasing at different V_b. The red line corresponds to the J–V characteristics after the pre-biasing at 1 V, the orange line corresponds to the pre-biasing at 1.5 V, and the yellow line corresponds to the J–V characteristics after the pre-biasing at 2 V. The increase of V_b leads to a shift of the "kink" to the low voltage region, as well as to the lowering of the V_{th} value and earlier observation of EL (Fig. 2a). The applying of the higher V_b results in a more pronounced p–i–n structure inside the perovskite layer owing to the accumulation of larger amount of ions at the perovskite interfaces. The formation of the p–i–n structure occurs in several seconds (Fig. S3, ESI†), and each V_b demonstrates that the saturated value of V_{th} shifted to the low voltage region (Fig. S4, ESI†).

Moreover, the increase of V_b also leads to a higher amplitude of EL. The EL ignition occurs in the low voltage region,

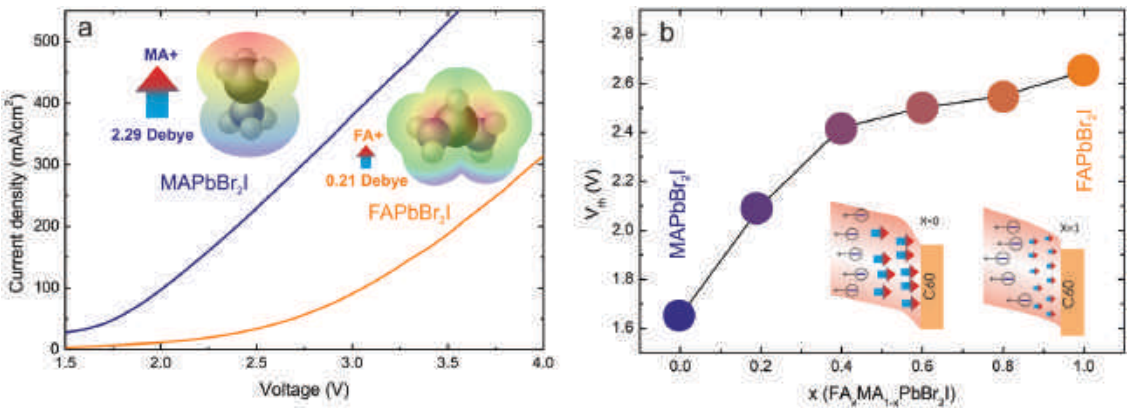

Fig. 1 Ion migration in JV. (a) J–V curves of MA- and FA-based perovskite devices after pre-biasing at 1.5 V. Molecules of MA (2.29 Debye) have greater dipole moments than FA (0.21 Debye). Therefore, MA-based devices have stronger band bending and consequently, lower V_{th} than the FA-based devices. (b) Dependence of V_{th} on the cation composition of the mixed halide perovskite. The values of V_{th} were obtained from a linear approximation of the J–V characteristics after several pre-biasings of the devices at 1.5 V for 1 minute in the dark. The inset demonstrates the probable band bending for the devices based on $MAPbBr_2I$ (x = 0) and $FAPbBr_2I$ (x = 1).

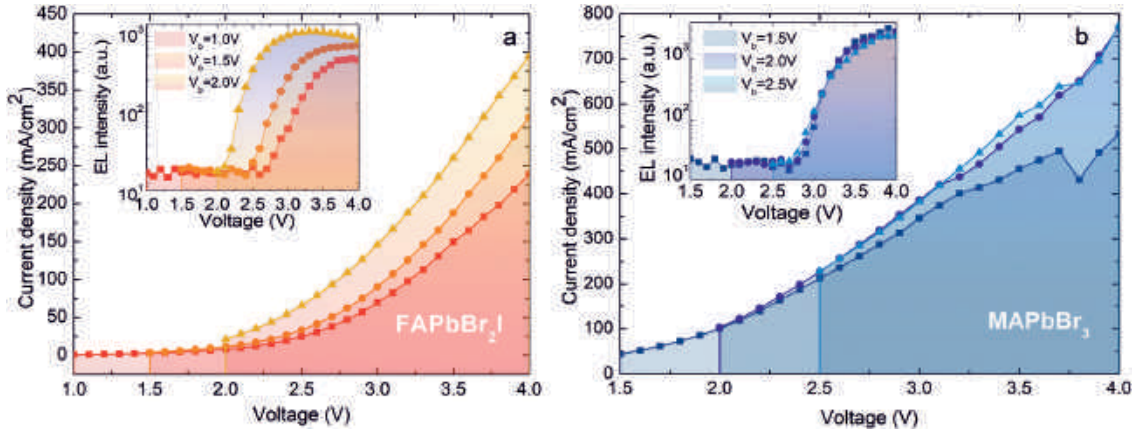

Fig. 2 Biasing the mixed halide and monohalide perovskite devices. (a) J–V characteristics of the $FAPbBr_2I$-based device after different pre-biasing voltages (V_b = 1, 1.5, 2 V). Inset shows the behavior of EL amplitude after biasing under different V_b. (b) J–V characteristics of $MAPbBr_3$ based device after pre-biasing at different voltages. Inset demonstrates corresponding EL peak intensity after pre-biasing at different voltages.

which reflects the better charge injection conditions upon increasing V_b (inset in Fig. 3a) as a result of the p–i–n structure build-up. The devices with different cation compositions demonstrate different V_{th} values after pre-biasing at equal V_b. This behavior of the V_{th} dependence (Fig. 1b) and high total difference between the V_{th} of the MA- and FA-based perovskites is quite surprising, and can be attributed to different dipole moments of the perovskite organic cations.[40] In addition, we measured the optical power of the devices in the LED regime, which is much lower for the case of the FA-based perovskite, as compared with that for the MA-based (Fig. S5a, ESI†). The LED emission line did not demonstrate any unusual behavior, and all devices exhibit EL in the red region (Fig. S6, ESI†) with the dependence of the peak position on FA_xMA_{1-x} ($0 \leq x \leq 1$) composition.

It is well known that the anion segregation induced by high current injection creates domains enriched with iodine ions inside the perovskite layer, and these domains determine the line position of EL.[15] In this regard, one can assume that the segregation should lower V_{th} due to the formation of I-rich regions, because the $FAPbBr_2I$-based device demonstrates EL around 785 nm (band gap around 1.58 eV) and the $MAPbBr_2I$ device demonstrates EL around 725 nm (band gap around 1.71 eV). In other words, if V_{th} lowering would be due to the formation of I-rich regions, the V_{th} value for the FA-based perovskite would be smaller than that of the MA-based perovskite. However, in our experiments, we observed the opposite result, where the FA-based perovskite demonstrated much higher V_{th} ($\approx$2.62 V) than the MA-based perovskite ($\approx$1.68 V). It indicates that I-rich regions do not considerably affect V_{th} of the mixed halide based LESC. This could arise from the partial coverage of the perovskite grains by the segregated regions, according to the work in ref. 43, where the $MAPbBr_2I$ perovskite had only 45% coverage with segregated regions. This does not support the charge carrier propagation between the electrodes in bypass of the host perovskite.

We also conducted the same cycle of biasing with the monohalide-based perovskite devices. We investigated the $MAPbBr_3$-based LESC of the same device design because it also has a high potential barrier for electron injection (Fig. S7, ESI†).

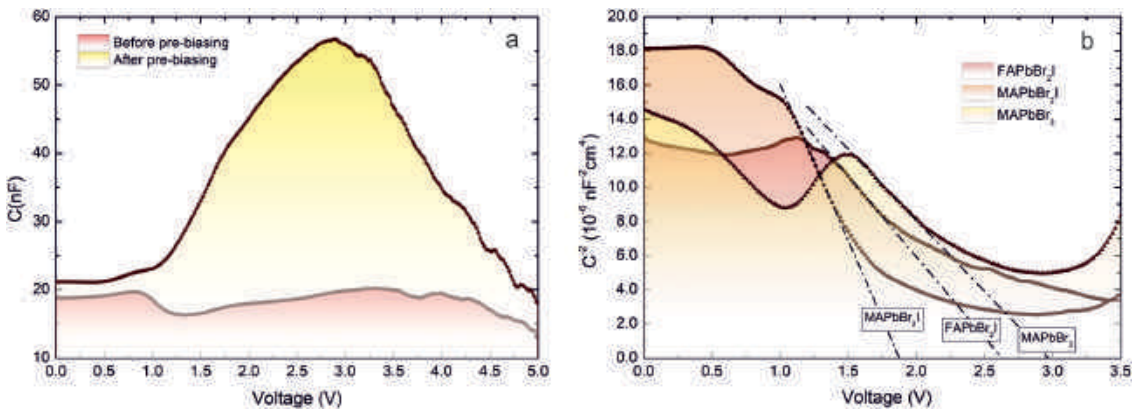

Fig. 3 C–V characteristics of the perovskite dual functional devices. (a) C–V characteristics before (black line) and after (red line) pre-biasing the device. (b) Mott–Schottky curves of the pre-biased dual functional devices based on $MAPbBr_2I$, $FAPbBr_2I$ and $MAPbBr_3$. The linear approximation gives the V_{bi} values of the devices.

Fig. 2b shows the obtained *J–V*, EL–*V* characteristics for the $MAPbBr_3$-based dual functional device. The *J–V* characteristics of the $MAPbBr_3$-based device do not demonstrate behaviors similar to the mixed halide perovskite upon prebiasing even after biasing at high voltages (V_b = 1.5, 2.0 and 2.5 V). The absence of the shift in *J–V* (Fig. 3b) and EL–*V* (inset in Fig. 3b) after biasing at V_b = 1.5, 2.0, and 2.5 V corresponds to extremely slow MA^+-ion movement under the applied voltage. Otherwise, these characteristics would demonstrate a considerable shift to the lower voltages and increase of the EL intensity in a sequence of measurements (inset in Fig. 2b). This is in good agreement with the work,[33] where the device barely demonstrated EL without the PEI layer between the perovskite and electrode. Although there is a small shift in the *J–V* and EL–*V* characteristics (Fig. 2b), it can be attributed to the movement of the Br^- ions and formation of a weak p–i–n structure. This correlates with the investigations of halide diffusion in $MAPbI_3$[35,36,44] and $MAPbBr_3$, where the perovskite demonstrated a high diffusion coefficient of the I^- and Br^- ions ($D \approx 10^{-9}$ cm^2 s^{-1}) and extremely low diffusion coefficient of MA^+ ion ($D \approx 10^{-12}$ cm^2 s^{-1}).[35,36,44,45] Therefore, the p–i–n structure in the monohalide perovskites forms mainly due to the I^- or Br^- ions and their vacancies.[36,44] This should not be enough to achieve the strong band structure bending to overcome the high potential barriers, and enhance the charge injection efficiency in the LED working regime without the use of any special electrode work function-modifying layers. As a result, one can assume that in the case of mixed halide perovskites, both anions and cations move under the applied external voltage or light illumination.

Generally, ionic migration in halide perovskites occurs with higher probability *via* such pathways as Frenkel and Shottky defects, lattice distortion by impurities, accumulated charges and lattice softening due to illumination, or even the piezoelectric effect.[13] Thus, one of the possible reasons for the ionic movement being more pronounced in mixed halide perovskites than in monohalides originates from these segregation-related processes. For example, since the grains of the mixed halide perovskite have Br- and I-rich domains, it can lead to an even more distorted lattice inside the perovskite grain. This is because the Br-rich domain with the smaller lattice parameter is placed in the center of the grain, while the I-rich domain is placed at the border of the grain.[46] Additional lattice disturbances might occur due to the gradient of a lattice parameter in the perovskite grain, and this can lead to even higher softening of the perovskite lattice, which can increase the diffusion coefficient of the cations. Our arguments are supported by previous calculations,[47] which demonstrated that the mixed halide and mixed cation perovskites can build up domains enriched with one cation. Nevertheless, this topic needs further experimental and theoretical investigations for clarifying the origin of the ionic migration pathways in the mixed halide perovskites.

For accurate determination of the built-in voltage, we conducted measurements of the capacitance–voltage characteristics of the LESCs in the LED regime. Fig. 3a demonstrates the obtained *C–V* characteristics before and after pre-biasing of the dual functional devices based on $MAPbBr_2I$ (Fig. S8, ESI† shows the *C–V* characteristics for the devices based on $MAPbBr_2I$, $FAPbBr_2I$ and $MAPbBr_3$). The orange curve in Fig. 3a corresponds to the unbiased device, and the black one corresponds to the device biased at 1.5 V for 1 minute. The presence of a "kink" and the increased capacitance on the black curve corresponds to the charge accumulation and formation of the p–i–n structure inside the perovskite layer.[48] The Mott–Schottky analysis[49] of the obtained *C–V* characteristics for the devices based on $MAPbBr_2I$, $FAPbBr_2I$, $MAPbBr_3$ gave the values of V_{bi} around 1.7, 2.6 and 2.9 V (Fig. 3b), which are in good agreement with those obtained from the LED *J–V* characteristics[48] (Fig. 2 and 3).

The optical power output of the perovskite LESCs strongly depends on such parameters like the potential barrier height, parameters of transport layers, and surface recombination. The use of a perovskite with a lower band gap ($MAPbBrI_2$) leads to the increase of the optical power output since the potential barrier between the perovskite and transport layers is lower than that for the $MAPbBr_2I$ perovskite (Fig. S5a, ESI†). The use of an alternative electron transport material, for example $PC_{60}BM$ (Fig. S5b and c, ESI†), improves the LESC emitting performance. It is well known that $PC_{60}BM$ possesses much better electronic properties[50] than C60. Also, the $PC_{60}BM$ transport layer decreases the amount of surface states, which dramatically enhances the device performance.[51] Therefore, the use of the $PC_{60}BM$ transport layer in the LESC leads to the increase of the optical power output (Fig. S5b, ESI†) and lowering of the amount of leakage current in the device owing to the passivation of surface states that enables the achievement of optical power output around 60 μW even in the highly non-optimized device design that yields an efficiency of ≈0.1% (Fig. S5c, ESI†), as in the case of the polyelectrolyte ETL.[33] Therefore, the formation of the p–i–n structure inside the perovskite layer and accumulation of organic cation molecules at the perovskite/ETL interface help to modify the device band structure, and achieve high optical power output from the SC device design.

Fig. 4 shows schematically how the ionic migration in the perovskites helps to modify the device band diagram, where the voltage pre-biasing plays an important role in the achievement of low V_{th} of the LED regime. We suggest that during the pre-biasing, the anions and cations move towards the perovskite/transport layer interfaces under applied voltage and form accumulation layers (Fig. 4). The anion and cation accumulation layers at the perovskite interfaces can work as electronic double layers (EDLs) formed at the HTL/perovskite and perovskite/ETL interfaces. These EDLs pin the Fermi level of ETL and HTL with p- and n-doped regions of the perovskite layer like in the light-emitting electrochemical cells (LECs).[52,53] Here, the ions of the dopant Li-salt, *e.g.*, $LiPF_6$, move towards the emission layer interface and form EDLs, achieving Ohmic contact and improving the charge injection into the emission layer. Thus, the presence of cation and anion EDLs in the perovskite improves charge injection into the perovskite layer, allowing EL manifestation.

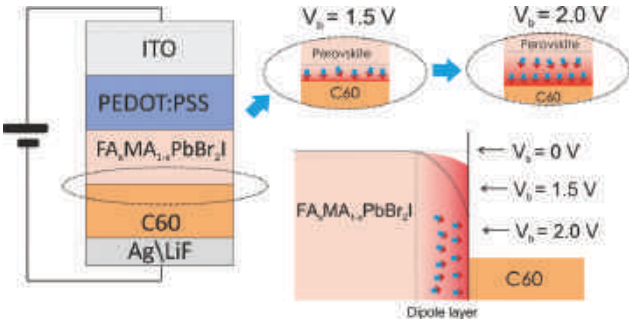

Fig. 4 Device band bending model. Schematic illustration of the cation migration during the device pre-biasing (anions omitted for simplicity). The pre-biasings at different V_b lead to the accumulation of cations at the perovskite\C60 layer. Higher V_b leads to higher cation density at the interface. As a result, the device will have different V_{th} values because the different cation densities induce different device band bending.

As a result, we propose that in the mixed halide perovskites, the non-zero dipole moment of the organic cations should also be taken into account. This is because the accumulation layer of the organic cations at the perovskite/C60 interface will also cause additional bend bending in this case due to its high dipole moment. In this case, the cation accumulation layer works as a polyelectrolyte or dipole layer and modifies the device band structure for LED operation, allowing for the achievement of low V_{th} and relatively high LED efficiency.[33,41,54] The band bending also depends on the amount of accumulated cations at the perovskite/C_{60} interface during the device pre-biasing (Fig. 2a). The higher value of V_b results in lower V_{th} (Fig. 3a) due to the formation of a stronger accumulation layer (Fig. 4). Since MA^+ and FA^+ have different dipole moments, it results in different V_b values needed to bend the band diagram and achieve low V_{th} (Fig. 2 and 4). The dipole moment of the MA^+ molecule is comparable to the dipole moments of ETL widely used in organic light emitting diodes like BCP and TPBI.[48] Therefore, the ionic migration of both cations and anions, the formation of EDLs, and the high dipole moment of an organic cation make the mixed halide perovskite more prospective than the monohalide ones for the development of LESC.

Conclusions

We have demonstrated that the ionic migration in mixed halide perovskites helps to modify the device band structure, which allows for switching the SC-preferable band diagram to an LED-preferable one due to the formation of cation and anion accumulation layers. Based on the experimental results, we assume that since the perovskite organic MA^+ and FA^+ cations have high non-zero dipole moments of 2.29 and 0.21 Debye, respectively, the organic-based accumulation layer bends the device band structure more than those formed by the anions. Thus, the formation of accumulation layers becomes possible under the applied voltage, and can lead to the p–i–n structure build up inside the perovskite layer during the device pre-biasing. The band bending due to the cation accumulation layer allows for overcoming the high potential barrier between the perovskite and transport layers in a standard solar cell design with the use of PEDOT:PSS and C60 as transport layers. Thus, the device band diagram can be controllably switched from a solar cell to LED operation. For example, in the case of the $MAPbBr_2I$ perovskite, the V_{th} value can be as low as 1.7 V. In contrast, the $FAPbBr_2I$ perovskite supports V_{th} = 2.6 V, and the $MAPbBr_3$ perovskite barely reaches V_{th} = 2.9 V. Therefore, for the creation of the dual functional device, the mixed halide perovskites are more prospective than the monohalide ones due to both cation and anion migration.

Materials and methods

Device fabrication

The following scheme was chosen for the functional layers ITO/PEDOT:PSS/$FA_xMA_{1-x}PbBr_2I$/C_{60}/LiF/Ag. The device functional layers were subsequently deposited onto the ITO-covered glass substrates. Glass substrates with ITO were consequently cleaned in an ultrasound bath in deionized water, acetone and isopropyl alcohol. Dried substrates were exposed to UV irradiation (189, 254 nm) for 900 s. Water dispersion of PEDOT:PSS 4083 was used as a HTL. It was filtered through a PTFE 0.45 syringe filter and deposited by spin coating. After spin coating, the film was annealed on a heating plate for 10 min at 150 °C. A photoactive layer based on $FA_xMA_{1-x}PbBr_2I$ and MAPbBr3 was prepared by the subsequent dissolving of methylammonium formamidinium iodide or methylammonium bromide (MAI, FAI, MABr, DyeSol), and lead(II) bromide ($PbBr_2$, Alfa Aesar "Puratronic" 99,999%) in a mixture of dimethylformamide (DMF) and dimethyl sulfoxide (DMSO) in a ratio of DMF : DMSO (7 : 3), respectively. The solutions were stirred overnight at room temperature. The acquired perovskite inks were deposited by the single step solvent engineering technique on top of HTL in a 2-step spin-cycle inside the glovebox system with nitrogen atmosphere. Anhydrous diethyl ether was used as an antisolvent, and was slowly dripped on the rotating substrate in 10 s past the jump from 500 to 3000 rpm. The acquired perovskite films were subjected to vacuum annealing for 1 min with subsequent annealing on the heating plate at 100 °C for 10 minutes. $PC_{60}BM$ (Lumteck) and C_{60} (Sigma-Aldrich) were used as ETL. C_{60}, LiF and Ag layers were deposited by thermal evaporation. The $PC_{60}BM$ solution in chlorobenzene (99.8% anhydrous, Sigma-Aldrich) with a concentration of 20 mg ml^{-1} was prepared inside the glove box. Prior to deposition, the $PC_{60}BM$ solution was filtered through the 0.45 μm PTFE filter and was deposited by spin coating (1000 rpm for 60 s). After $PC_{60}BM$ deposition, the devices were annealed at 100 °C for 15 minutes.[51]

Device characterization

A solar simulator (Asahi Spectra HAL-320) with calibrated 1.5 AM G solar spectrum and source-meter unit (Keithley 2400) were used for the solar cell characterization. Capacitance–voltage measurements were performed by LCR-meter (Agilent E4980A) at a

frequency of 1 kHz. Electroluminescence spectra were measured by a spectrometer (Avantes AvaSpec-Mini4096CL). The optical power was measured by an optical power meter (Ophir Nova 2).

Conflicts of interest

There are no conflicts of interest to declare.

Acknowledgements

This work was supported by the Russian Science Foundation (project No. 19-73-30023).

References

1 N. Park, *Adv. Energy Mater.*, 2020, **10**, 1903106.
2 S. Akin, N. Arora, S. M. Zakeeruddin, M. Grätzel, R. H. Friend and M. I. Dar, *Adv. Energy Mater.*, 2020, **10**, 1903090.
3 M. Lu, Y. Zhang, S. Wang, J. Guo, W. W. Yu and A. L. Rogach, *Adv. Funct. Mater.*, 2019, **29**, 1902008.
4 Z. Liu, L. Krückemeier, B. Krogmeier, B. Klingebiel, J. A. Márquez, S. Levcenko, S. Öz, S. Mathur, U. Rau, T. Unold and T. Kirchartz, *ACS Energy Lett.*, 2019, **4**, 110–117.
5 S. D. Stranks, R. L. Z. Z. Hoye, D. Di, R. H. Friend and F. Deschler, *Adv. Mater.*, 2019, **31**, 1803336.
6 M. Jung, S. G. Ji, G. Kim and S. Il Seok, *Chem. Soc. Rev.*, 2019, **48**, 2011–2038.
7 M. A. Becker, R. Vaxenburg, G. Nedelcu, P. C. Sercel, A. Shabaev, M. J. Mehl, J. G. Michopoulos, S. G. Lambrakos, N. Bernstein, J. L. Lyons, T. Stöferle, R. F. Mahrt, M. V. Kovalenko, D. J. Norris, G. Rainò and A. L. Efros, *Nature*, 2018, **553**, 189–193.
8 W. S. Yang, B. Park, E. H. Jung, N. J. Jeon, Y. C. Kim, D. U. Lee, S. S. Shin, J. Seo, E. K. Kim, J. H. Noh and S. Il Seok, *Science*, 2017, **356**, 1376–1379.
9 D. P. McMeekin, G. Sadoughi, W. Rehman, G. E. Eperon, M. Saliba, M. T. Hörantner, A. Haghighirad, N. Sakai, L. Korte, B. Rech, M. B. Johnston, L. M. Herz and H. J. Snaith, *Science*, 2016, **351**, 151–155.
10 S. Il Seok, M. Grätzel and N. Park, *Small*, 2018, **14**, 1704177.
11 K. Lin, J. Xing, L. N. Quan, F. P. G. de Arquer, X. Gong, J. Lu, L. Xie, W. Zhao, D. Zhang, C. Yan, W. Li, X. Liu, Y. Lu, J. Kirman, E. H. Sargent, Q. Xiong and Z. Wei, *Nature*, 2018, **562**, 245–248.
12 M. C. Brennan, S. Draguta, P. V. Kamat and M. Kuno, *ACS Energy Lett.*, 2018, **3**, 204–213.
13 Y. Yuan and J. Huang, *Acc. Chem. Res.*, 2016, **49**, 286–293.
14 E. T. Hoke, D. J. Slotcavage, E. R. Dohner, A. R. Bowring, H. I. Karunadasa and M. D. McGehee, *Chem. Sci.*, 2015, **6**, 613–617.
15 I. L. Braly, R. J. Stoddard, A. Rajagopal, A. R. Uhl, J. K. Katahara, A. K. Jen and H. W. Hillhouse, *ACS Energy Lett.*, 2017, **2**, 1841–1847.
16 D. J. Slotcavage, H. I. Karunadasa and M. D. McGehee, *ACS Energy Lett.*, 2016, **1**, 1199–1205.
17 A. J. Knight, A. D. Wright, J. B. Patel, D. P. McMeekin, H. J. Snaith, M. B. Johnston and L. M. Herz, *ACS Energy Lett.*, 2019, **4**, 75–84.
18 N. Aristidou, C. Eames, I. Sanchez-Molina, X. Bu, J. Kosco, M. S. Islam and S. A. Haque, *Nat. Commun.*, 2017, **8**, 15218.
19 C. Besleaga, L. E. Abramiuc, V. Stancu, A. G. Tomulescu, M. Sima, L. Trinca, N. Plugaru, L. Pintilie, G. A. Nemnes, M. Iliescu, H. G. Svavarsson, A. Manolescu and I. Pintilie, *J. Phys. Chem. Lett.*, 2016, **7**, 5168–5175.
20 C. Eames, J. M. Frost, P. R. F. Barnes, B. C. O'Regan, A. Walsh and M. S. Islam, *Nat. Commun.*, 2015, **6**, 7497.
21 E. C. Smith, C. L. C. Ellis, H. Javaid, L. A. Renna, Y. Liu, T. P. Russell, M. Bag and D. Venkataraman, *J. Phys. Chem. C*, 2018, **122**, 13986–13994.
22 S. N. Habisreutinger, N. K. Noel and H. J. Snaith, *ACS Energy Lett.*, 2018, **3**, 2472–2476.
23 D. W. Ferdani, S. R. Pering, D. Ghosh, P. Kubiak, A. B. Walker, S. E. Lewis, A. L. Johnson, P. J. Baker, M. S. Islam and P. J. Cameron, *Energy Environ. Sci.*, 2019, **12**, 2264–2272.
24 J. J. Yoo, S. Wieghold, M. C. Sponseller, M. R. Chua, S. N. Bertram, N. T. P. Hartono, J. S. Tresback, E. C. Hansen, J. P. Correa-Baena, V. Bulović, T. Buonassisi, S. S. Shin and M. G. Bawendi, *Energy Environ. Sci.*, 2019, **12**, 2192–2199.
25 T. H. Han, S. Tan, J. Xue, L. Meng, J. W. Lee and Y. Yang, *Adv. Mater.*, 2019, **1803515**, 1–35.
26 M. Hu, C. Bi, Y. Yuan, Y. Bai and J. Huang, *Adv. Sci.*, 2015, **3**, 6–11.
27 A. Walsh and S. D. Stranks, *ACS Energy Lett.*, 2018, **3**, 1983–1990.
28 Y. Deng, Z. Xiao and J. Huang, *Adv. Energy Mater.*, 2015, **5**, 1500721.
29 J.-W. Lee, S.-G. Kim, J.-M. Yang, Y. Yang and N.-G. Park, *APL Mater.*, 2019, **7**, 041111.
30 B. M. D. D. Puscher, M. F. Aygüler, P. Docampo and R. D. Costa, *Adv. Energy Mater.*, 2017, **7**, 1602283.
31 T. Zhang, S. H. Cheung, X. Meng, L. Zhu, Y. Bai, C. H. Y. Ho, S. Xiao, Q. Xue, S. K. So and S. Yang, *J. Phys. Chem. Lett.*, 2017, **8**, 5069–5076.
32 D. Gets, D. Saranin, A. Ishteev, R. Haroldson, E. Danilovskiy, S. Makarov and A. Zakhidov, *Appl. Surf. Sci.*, 2019, **476**, 486–492.
33 H. Kim, Y. J. Yoon, J. Jeong, J. Heo, H. Jang, J. H. Seo, B. Walker and J. Y. Kim, *Energy Environ. Sci.*, 2017, **10**, 1950–1957.
34 L. Gil-Escrig, G. Longo, A. Pertegás, C. Roldán-Carmona, A. Soriano, M. Sessolo and H. J. Bolink, *Chem. Commun.*, 2015, **51**, 569–571.
35 A. Senocrate, I. Moudrakovski, T. Acartürk, R. Merkle, G. Y. Kim, U. Starke, M. Grätzel and J. Maier, *J. Phys. Chem. C*, 2018, **122**, 21803–21806.
36 M. H. Futscher, J. M. Lee, L. McGovern, L. A. Muscarella, T. Wang, M. I. Haider, A. Fakharuddin, L. Schmidt-Mende and B. Ehrler, *Mater. Horiz.*, 2019, **6**, 1497–1503.
37 T. Chiba, D. Kumagai, K. Udagawa, Y. Watanabe and J. Kido, *Sci. Rep.*, 2018, **8**, 11472.

38 M. F. Aygüler, B. M. D. D. Puscher, Y. Tong, T. Bein, A. S. Urban, R. D. Costa and P. Docampo, *J. Phys. D: Appl. Phys.*, 2018, **51**, 334001.
39 Y. Liu, P. M. Hangoma, V. Tamilavan, I. Shin, I. W. Hwang, Y. K. Jung, B. R. Lee, J. H. Jeong, S. H. Park and K. H. Kim, *Nano Energy*, 2019, **61**, 251–258.
40 J. M. Frost, K. T. Butler, F. Brivio, C. H. Hendon, M. van Schilfgaarde and A. Walsh, *Nano Lett.*, 2014, **14**, 2584–2590.
41 Y. Zhou, C. Fuentes-Hernandez, J. Shim, J. Meyer, A. J. Giordano, H. Li, P. Winget, T. Papadopoulos, H. Cheun, J. Kim, M. Fenoll, A. Dindar, W. Haske, E. Najafabadi, T. M. Khan, H. Sojoudi, S. Barlow, S. Graham, J.-L. Bredas, S. R. Marder, A. Kahn and B. Kippelen, *Science*, 2012, **336**, 327–332.
42 W.-J. Yin, T. Shi and Y. Yan, *Appl. Phys. Lett.*, 2014, **104**, 063903.
43 J. Cho and P. V. Kamat, *Chem. Mater.*, 2020, **32**, 6206–6212.
44 L. McGovern, M. H. Futscher, L. A. Muscarella and B. Ehrler, *J. Phys. Chem. Lett.*, 2020, **11**, 7127–7132.
45 G. M. Bernard, R. E. Wasylishen, C. I. Ratcliffe, V. Terskikh, Q. Wu, J. M. Buriak and T. Hauger, *J. Phys. Chem. A*, 2018, **122**, 1560–1573.
46 W. Li, M. U. Rothmann, A. Liu, Z. Wang, Y. Zhang, A. R. Pascoe, J. Lu, L. Jiang, Y. Chen, F. Huang, Y. Peng, Q. Bao, J. Etheridge, U. Bach and Y. B. Cheng, *Adv. Energy Mater.*, 2017, **7**, 1–8.
47 K. P. McKenna, *ACS Energy Lett.*, 2018, **3**, 2663–2668.
48 Y. Noguchi, Y. Miyazaki, Y. Tanaka, N. Sato, Y. Nakayama, T. D. Schmidt, W. Brütting and H. Ishii, *J. Appl. Phys.*, 2012, **111**, 114508.
49 O. Almora, C. Aranda, E. Mas-Marzá and G. Garcia-Belmonte, *Appl. Phys. Lett.*, 2016, **109**, 173903.
50 N. B. Kotadiya, A. Mondal, P. W. M. Blom, D. Andrienko and G.-J. A. H. Wetzelaer, *Nat. Mater.*, 2019, **18**, 1182–1186.
51 Y. Shao, Z. Xiao, C. Bi, Y. Yuan and J. Huang, *Nat. Commun.*, 2014, **5**, 1–7.
52 M. H. Bowler, A. Mishra, A. C. Adams, C. L. D. Blangy and J. D. Slinker, *Adv. Funct. Mater.*, 2020, **1906715**, 1–13.
53 K. Youssef, Y. Li, S. O'Keeffe, L. Li and Q. Pei, *Adv. Funct. Mater.*, 2020, **1909102**, 1909102.
54 X. Peng, L. Hu, F. Qin, Y. Zhou and P. K. Chu, *Adv. Mater. Interfaces*, 2018, **5**, 1701404.